Modeling Hypervelocity-impact-induced Shock Waves for Characterizing Orbital Debris-produced Damage

Menglong Liu[# a], Zhongqing Su[* a], Qingming Zhang [b], Renrong Long [b]

[a]Department of Mechanical Engineering, The Hong Kong Polytechnic University
Kowloon, Hong Kong

[b]State Key Laboratory of Explosion Science and Technology, Beijing Institute of Technology
Haidian District, Beijing, 100081, P. R. China

Submitted to *JOURNAL of APPLIED MECHANICS*

(initially submitted on 8 December 2015; revised and re-submitted on 29 March 2016)

PhD student

∗ Corresponding author. Tel.: +852-2766-7818; fax: +852-2365-4703. Email: zhongqing.su@polyu.edu.hk (Prof. Zhongqing Su, *Ph.D.*)

Abstract

Hypervelocity impact (HVI) is a scenario involving an impacting velocity in excess of 1 km/s. Ubiquitous in outer space, paradigms of HVI are typified by the collision between orbital debris and spacecraft. HVI features transient, localized, and extreme material deformation, under which the induced acoustic emission (AE) signals present unique yet complex features. A dedicated modeling and numerical simulation approach, based on the three-dimensional smooth-particle hydrodynamics (SPH), was developed to gain an insight into characteristics of HVI-induced AE propagation. With the approach, both normal and oblique HVI scenarios were interrogated, and material failure in both cases was predicted. The coincidence in results between simulation and HVI experiment, as observed at a qualitative degree, has demonstrated the effectiveness of the modeling. Signal analysis shows that the shock wave converts to Lamb wave quickly as propagation from HVI spot, with the zeroth-order symmetric wave mode (S_0) (*i.e.*, the first-arrival wave) dominating wave signal energy. S_0 is observed dispersive in a wide frequency range with majority of it below 1 MHz. In comparison, the anti-symmetric wave mode distributes in a range below 200 kHz with a peak value at 30 kHz. S_0 was employed to pinpoint the location of HVI, using an enhanced delay-and-sum-based diagnostic imaging algorithm, which was validated by locating orbital debris-induced orifice in space structures, showing precise identification results.

1. Introduction

Near-Earth space, where numerous spacecraft (*e.g.*, satellites, space stations, and shuttles) orbit, is cluttered with meteoroids and orbital debris (MODs). MODs travel at such high speeds (of the order of the first cosmic velocity) that even a small particle, if not evaded, can impact the spacecraft severely [1-3]. This sort of impact is commonly referred to as "hypervelocity impact" (HVI) – a scenario typically involving an impacting velocity in excess of 1 km/s. HVI is ubiquitous in space, as evidenced by the millions of impact lesions to be seen on spacecraft after every flight mission.

Depending on the size and impact location, MODs-committed damage in space structures can take a variety of modalities, including recrystallization, cell dislocation, micro-cracks, microband extension, material vaporization, cratering, spall cracks, plastic zones, and macroscopic penetration, to name a few [4-6]. MODs, when less than 100 μm in size, may not produce visible cratering, but barely visible micro-cracks can be initiated; when reaching one-tenth millimeter, they can give rise to surface erosion; any MOD over 1 cm is large enough to penetrate any shielding layer of spacecraft. Even if not immediate, the generated damage in spacecraft deteriorates at an alarming rate in space environments, soon reaching a critical level and leading to mission failure without sufficient warning [7].

According to NASA, ~19,000 pieces of orbital debris larger than 10 cm, ~500,000 sized 1~10 cm, and tens of millions smaller than 1 cm, are known to exist in low Earth and geosynchronous orbits. The impact from any of them can functionally compromise the craft performance, with possibly catastrophic consequences. Representatively, in 2009 a satellite in the Iridium Communications Constellation System was struck by the debris generated from an exploded satellite which was abandoned by then Soviet, and this

satellite failed immediately [8]. Notably, this HVI event created approximately 2,000 new pieces of debris, posing severer HVI risk to other space assets on the orbits.

To minimize HVI hazard to orbiting spacecraft, a diversity of shielding mechanisms (*e.g.*, Whipple shield [9], stuffed Whipple shield [9], and multi-shock shield [10]) have been developed and installed on space assets, especially for those with a requirement of long service period or with habitation of astronauts. With them, space assets are expected to survive upon HVI from MODs. Addressing such significance, HVI has received a great deal of attention over the years and from the 1950s in particular when human beings began extensive exploration into the outer space [11]. The importance and necessity of evaluating HVI-induced damage in space assets in an accurate, precise and prompt manner cannot be overemphasized. With timely evaluation, further deterioration of the damaged structures could be prevented through remediation, so as to weaken the risk of consequent system failure. Inspired by such an imperative need, a variety of sensing and diagnosis techniques has been deployed, to perceive HVI events and accordingly estimate the severity of HVI-committed damage [7].

In such a context, acoustic emission (AE) - the phenomenon of radiation of acoustic energy disseminating in solids when a material undergoes irreversible changes in its internal structure - plays a substantial role to sense HVI signals and locate HVI spot. Most AE-based triangulation algorithms solve localization equations according to the difference in arrival time of two AE signals captured via two sensing paths [12, 13], whereby the acoustic source (*i.e.*, the HVI spot) can be inversely positioned using classical AE analysis as elaborated in [12, 13]. Beamforming is another localization method to fulfill such a localization task [14, 15], making use of the synchronization of guided waves created by a

89 phased array consisting of a number of transducers which are sequentially activated. In
90 implementation, these algorithms entail the following presumptions: (1) the velocity of
91 HVI-induced wave is constant; (2) the wave mode is haploid; and (3) wave dispersion can
92 be largely ignored. These approaches are demonstrably effective and precise in
93 low-velocity impact (LVI) cases.
94
95 As opposed to numerous studies pertaining to LVI as well as detection of LVI-induced
96 damage [16], insofar as observed, a very limited number of researches have been focused
97 on the shock waves generated under HVI, let alone the use of them for damage evaluation.
98 Prosser *et al.* [17] experimentally compared AE signals captured in both LVI (less than
99 0.21 km/s) and HVI (1.8~7 km/s), and concluded that both the extensional and the flexural
100 wave modes co-exist in two impact cases. Compared with those under LVI, the structural
101 responses under HVI present much greater magnitudes in a wider frequency band. Perkins
102 [18] implemented a series of HVI experiments using Polyvinylidene fluoride (PVDF) as
103 AE sensors to acquire HVI-induced waves, and linked the changes in signal amplitude and
104 energy attenuation to the occurrence of impact damage. However, as pointed out in this
105 study, owing to the exorbitant sensitivity of PVDF to ambient conditions (*e.g.*, fluctuating
106 temperature), repeated tests showed low coincidence; and moreover, the sole use of signal
107 features in the frequency domain limited the approach from providing spatial information
108 on damage location. Targeting a quantitative prediction of the location of HVI spot,
109 Schäfer and Janovsky [19] attached acoustic transducer networks on a 2 mm thick
110 aluminum alloy panel and a 49 mm thick sandwich panel (both panels are target structures),
111 respectively. HVI spots in two panels were triangulated by assuming that HVI-induced
112 waves propagated at a constant velocity.
113

However, considerably different from LVI in which no shock waves are initiated, HVI releases much more concentrated energy within a shorter period, generating shock waves with unique yet complex features which are substantially distinct from those under LVI. Wave modes of various orders co-exist, propagating at distinct velocities and presenting complex dispersive and multi-modal natures, along with phase distortion. Nevertheless, regardless of the fundamental differences between LVI and HVI, most existing studies take it for granted that the triangulation algorithms used for LVI could be straightforwardly applied to HVI without a need of correction or compensation.

To comprehend the wave propagation under HVI, studies with a nature of theoretical analysis, numerical simulation, or experiment have been attempted. But, limited by great technical difficulties and high cost of HVI apparatuses which can accelerate a particle to move at 1 km/s or above, experimental work is fairly restricted. As an alternative, numerical simulation has been increasingly preferred. In this backdrop, the Eulerian and Lagrangian descriptions [20-22] are two major theoretical frameworks, defining the physical governing equations in finite difference (FD) and finite element (FE) [23], respectively. However, FD method features a fixed spatial grid in the entire space that the target structure traverses, and thus FD may fail to interpret HVI-induced shock waves because the Eulerian description can become inefficient and lead to singularity in the grid when a large deformation occurs like the cases in HVI; while an FE method may yield erroneous results, because HVI involves extremely distorted elements – beyond the computational capacity of FE. Restricted by these, conventional numerical modeling and simulation methods, based on either FD or FE, show their limitations in dealing with HVI. Together, these factors have imposed great challenge in faithfully understanding the

propagation of HVI-induced waves. Interpretation of shock waves and AE signals under HVI can be incorrect, if the classic theory of elasticity, conventional modeling, simulation, and experiment methods are used. Such difficulty can further downgrade the accuracy and precision of HVI localization.

In recognition of the bottleneck in today's scientific regime as addressed in the above, the current study is dedicated to fundamental understanding of propagation of HVI-induced shock waves, with an application to locating HVI-committed damage in space structures. A dedicated modeling and numerical simulation approach, based on the three-dimensional smooth-particle hydrodynamics (SPH) in conjunction with the FE analysis, was developed, with which both the normal and oblique HVI cases were investigated, and material failure in both cases was predicted. Using a diagnostic imaging algorithm, a localization strategy targeting orbital debris-committed orifice in space structures was developed and validated. This paper is organized as follows. Section 2 elucidates the theory and principle of the proposed modeling and simulation approach, as well as its numerical implementation. Two specific HVI scenarios – normal and oblique HVI, are explored and detailed in Section 3. An enhanced delay-and-sum-based imaging algorithm for visualizing HVI spot is proposed and validated in Section 4, followed with concluding remarks enumerated in Section 5.

2. Modeling Shock Waves under HVI

2.1. Theory and Principle

Significantly distinct from LVI, HVI features transient, localized, and extreme material deformation in a loading process involving material melting and distortion. The vicinity of HVI spot exhibits material traits between a fluid and a solid. It is a daunting task to reflect these traits faithfully using a conventional FD or FE method, as explicated previously.

A dedicated modeling and simulation approach based on the three-dimensional smooth-particle hydrodynamics (3D-SPH) was developed. SPH, originated for studying astrophysics and then brought to fluid dynamics (hydrodynamics) [24], has gained its popularity in astrophysics, hydrodynamics, and solid dynamics [25-27] in recent years, as reviewed elsewhere [28]. In 3D-SPH, a structure under investigation is first simplified and discretized with particles. Using particles (rather than "elements" as in FE), SPH is a meshless Lagrangian particle method, whose meshless nature endows the model with a capacity to mimic transient large material deformation. Without loss of the generality, for particle *i*, its deformation, denoted by $f(\mathbf{x})\big|_i$ (where $f(\mathbf{x})$ signifies particle deformation and $\mathbf{x}$ is the spatial vector) can be approximated in terms of the deformation of its neighboring particles ($j = 1, \cdots, N$) within a support domain Ω (a domain comprised of *N* particles), as

$$f(\mathbf{x})\big|_i \approx \sum_{j=1}^{N} f(\mathbf{x}_j) W(\mathbf{x}_i - \mathbf{x}_j) \Delta V_j = \sum_{j=1}^{N} f(\mathbf{x}_j) W(\mathbf{x}_i - \mathbf{x}_j) m_j / \rho_j, \quad (1)$$

where ΔV_j, m_j, and ρ_j are the volume, mass, and density of neighboring particle *j*, respectively. *W* is a smoothing function (to be detailed in Section 2.2). At each step of calculation, updated neighboring particles for particle *i* are searched first (because material undergoes extreme deformation during HVI and Ω may involve different numbers of particles at each step), and then the computation using Eq. (1) is carried out based on the updated Ω. Such a meshless modeling philosophy allows both the projectile and target structures to deform without a geometric constraint, and can therefore reflect material deformation under HVI faithfully. In addition, SPH in principle is a Lagrangian method, and there is no need to model the entire space like an Eulerian algorithm does.

187

188 On the other hand, because HVI makes part of the target structure behave like a fluid and
189 go through a high compression, modeling of wave propagation in the target structure lies
190 on the Navier-Stokes equation in this approach [29], which reads, in the absence of any
191 external force, as

192
$$\begin{aligned} \frac{D\rho}{Dt} &= -\rho\frac{\partial v^{\alpha}}{\partial x^{\alpha}}, \\ \frac{Dv^{\alpha}}{Dt} &= \frac{1}{\rho}\frac{\partial \sigma^{\alpha\beta}}{\partial x^{\beta}}, \\ \frac{De}{Dt} &= \frac{\sigma^{\alpha\beta}}{\rho}\frac{\partial v^{\alpha}}{\partial x^{\beta}}, \end{aligned} \tag{2}$$

193 where α and β ($\alpha,\beta=1,2,3$) are tensor indices; ρ, t, $\mathbf{v}$ (or v^{α}), $\boldsymbol{\sigma}$ (or $\sigma^{\alpha\beta}$), and
194 e are the density, time, velocity vector, stress tensor, and internal energy of an
195 infinitesimally small element moving with the flow, respectively; D denotes partial
196 differential in Lagrangian description.

197

198 Combining the physical equations describing shock wave propagation (Eq. (2)) and
199 3D-SPH algorithm (Eq. (1)) leads to, for particle i over Ω,

200
$$\begin{aligned} \frac{D\rho_i}{Dt} &= \sum_{j=1}^{N} m_j (v_i^{\alpha} - v_j^{\alpha})\cdot\frac{\partial W(x_i - x_j)}{\partial x_i^{\alpha}}, \\ \frac{Dv_i^{\alpha}}{Dt} &= \sum_{j=1}^{N} m_j \left(\frac{\sigma_i^{\alpha\beta}}{\rho_i^2} + \frac{\sigma_j^{\alpha\beta}}{\rho_j^2}\right)\cdot\frac{\partial W(x_i - x_j)}{\partial x_i^{\beta}}, \\ \frac{De_i}{Dt} &= \frac{1}{2}\sum_{j=1}^{N} m_j \frac{\rho_i + \rho_j}{\rho_i\rho_j}(v_i^{\beta} - v_j^{\beta})\frac{\partial W(x_i - x_j)}{\partial x_i^{\beta}} + \frac{1}{\rho_i}\tau_i^{\alpha\beta}\dot{\varepsilon}_i^{\alpha\beta}, \end{aligned} \tag{3}$$

201 where $\tau_i^{\alpha\beta}$ and $\dot{\varepsilon}_i^{\alpha\beta}$ are deviatoric stress and strain rate, respectively. The leapfrog
202 algorithm [30] was used in this study to solve Eq. (3). Equation (3) embraces three
203 conservation equations based on continuum mechanics, which is, however, inadequate to
204 solve all the unknown variables it involved. To circumvent this inadequacy, (i) equation of

205 state (EOS), (ii) strength model, and (iii) failure criterion were introduced to the modeling
206 as a supplement to Eq. (3), which are respectively illustrated as below.
207
208 **(i) *EOS for Shock Waves***
209 An EOS describes a relation between the pressure and the state variables of the material
210 (*e.g.*, the correlation between material compression ratio and internal energy under HVI).
211 The *Shock EOS* – a sort of EOS to deal with HVI – was used in the modeling. Consider the
212 stress responses ($\boldsymbol{\sigma}$ or $\sigma^{\alpha\beta}$) of the target structure, which can be defined, in continuum
213 mechanics, as the summation of hydrostatic pressure (p) and deviatoric stresses ($\boldsymbol{\tau}$ or
214 $\tau^{\alpha\beta}$), as

215 $$\sigma^{\alpha\beta} = -p\delta^{\alpha\beta} + \tau^{\alpha\beta}, \tag{4}$$

216 where $\delta^{\alpha\beta}$ is the Kronecker delta. The first term on the right-hand side of Eq. (4) is
217 associated with EOS, while the second term is linked to the strength model (to be
218 illustrated later). p is be correlated with density (ρ) and internal energy (e) via the
219 Mie-Grüneisen equation [31], as

220 $$\begin{aligned} p(\rho,e) &= [1-\frac{1}{2}\Gamma(\frac{\rho}{\rho_0}-1)]p_H(\rho) + \Gamma\rho e, \\ \Gamma\rho &= \Gamma_0\rho_0 = const. \end{aligned} \tag{5}$$

221 In the above "*0*" in subscript represents a reference state - the state before HVI (*i.e.*, prior
222 to shock front), otherwise the current state after HVI. With this, ρ_0 denotes the initial
223 material density prior to HVI. Γ is the Grüneisen parameter [31]. p_H denotes Hugoniot
224 pressure of the HVI-induced shock waves – the pressure immediately following the impact
225 (*i.e.*, immediately behind shock front). To ascertain p_H, first consider the normal
226 incidence in which $\boldsymbol{\sigma} = -p$ and $\mathbf{v} = v$ where p is the pressure due to material
227 compression; and then the HVI-induced shock waves prior to and behind the shock front

can be delineated using density, pressure and energy, with a Rankine-Hugoniot jump conditions [32] according to Eq. (2), as

$$\begin{aligned} &\rho_H = \rho_0(v_s - v_0)/(v_s - v_H), \\ &p_H - p_0 = \rho_0(v_H - v_0)(v_s - v_0), \\ &e_H - e_0 = (p_H + p_0)(1/\rho_0 - 1/\rho_H)/2 = (v_H - v_0)^2/2. \end{aligned} \tag{6}$$

In analogy to Eq. (5), "0" and "*H*" in subscript in Eq. (6) represent the state prior to and immediately behind the shock front, respectively, and thus v_0 and v_H denote the particle velocity prior to and immediately behind the shock front, respectively. v_s is the instantaneous propagation velocity of HVI-induced shock wave. As $v_0 = 0$ and $p_0 = 0$, Eq. (6) retreats to

$$p_H = v_s^2 \rho_0 - \frac{v_s^2 \rho_0^2}{\rho_H}. \tag{7}$$

Particularly, provided the impact velocity less than 8 km/s, v_s can be found as [32]

$$v_s = c_0 + s v_H, \tag{8}$$

where c_0 ($c_0 = \sqrt{K/\rho_0}$), K and s signify the bulk wave velocity, bulk modulus of the target structure and a constant associated with material properties, respectively. Substituting Eq. (8) into Eqs. (6) and (7) yields

$$p_H = \frac{\rho_0 c_0^2 (1 - \rho_0/\rho_H)}{(1 - s(1 - \rho_0/\rho_H))^2}. \tag{9}$$

Equation (9) defines a relationship between Hugoniot pressure and density for the HVI-induced shock waves. To combine Eqs. (9) and (5) leads to the correlation among pressure, density and internal energy, upon the occurrence of HVI, as

$$p(\rho, e) = \frac{[1 - \frac{1}{2}\Gamma(\frac{\rho_H}{\rho_0} - 1)]\rho_0 c_0^2 (1 - \frac{\rho_0}{\rho_H})}{(1 - s(1 - \frac{\rho_0}{\rho_H}))^2} + \Gamma \rho_H e. \tag{10}$$

Equation (10) is namely the *Shock EOS*, and was used in the modeling.

(ii) *Strength Model*

A strength model governs the deviatoric stress-strain relationship of a material, suggesting yielding conditions of the projectile and target structures. The Steinberg Guinan strength model [33], – a semi-empirical flow stress model which has been well demonstrated at high strain rates (greater than $10^5 s^{-1}$), was adopted in the modeling, which reads

$$
\begin{aligned}
&G = G_0\left\{1+(\frac{\bar{G}_p}{G_0})\frac{p}{\eta^{1/3}}+(\frac{\bar{G}_T}{G_0})(T-T_0)\right\}\\
&Y = Y_0\left\{1+(\frac{\bar{Y}_p}{Y_0})\frac{p}{\eta^{1/3}}+(\frac{\bar{G}_T}{G_0})(T-T_0)\right\}(1+\Theta\varepsilon_p)^n . \qquad (11)\\
&\textit{subject to}\\
&Y_0(1+\Theta\varepsilon_p)^n \le Y_{\max}
\end{aligned}
$$

Same as the above, subscript "*0*" indicates the reference state prior to the shock front, otherwise the current state after HVI. G, Y and ε_p are the shear modulus, yielding stress and effective plastic strain, respectively; T is the temperature (initially, T_0 = 300 K in this study); η, reflecting the degree of compression of the material, is defined as ρ/ρ_0; Θ and n are the work-hardening constant and exponent, both of which are related to material properties. $\bar{G}_p$ and $\bar{G}_T$ are the derivatives of G with regard to p and T, respectively; similarly, $\bar{Y}_p$ denotes the derivative of Y with regard to p; $Y_{\max}$ is the maximum yielding stress of the target structure. To address the highly localized heating phenomena that are inherent in an HVI event, the temperature T was ascertained in the modeling via

$$T = T_0 + \frac{e-e_0}{mC_v}, \qquad (12)$$

where m and C_v (defined in EOS) are the mass and heat capacity at a constant volume. In the modeling, it was hypothesized that at a high-strain rate, G increases as the increase of pressure or the decrease of temperature. In addition, the Bauschinger effect [33] was

particularly taken into account in the modeling, reflected by the term $(\frac{\bar{Y}_p}{Y_0})\frac{p}{\eta^{1/3}}$ in Eq. (11). Additionally, a melting temperature (T_{melt}) was defined by considering the material properties of the projectile and target structures, over which the projectile and target structures behave like a fluid in which both G and Y are zero. As an example, all these parameters are tabulated in **Table 1** for the case to be discussed.

(iii) ***Failure Criterion***

The failure criterion used in the modeling was the maximum principal tensile criterion. This criterion assumes that failure of the target structure is to be initiated when the principal tensile stress behind the shock front exceeds a pre-defined failure stress over which the material can endure compression deformation only.

Using the *Shock EOS*, *strength model* and *failure criterion* illustrated in the above, plus the three conservation equations defined by Eq. (3), the hydrostatic and deviatoric stresses behind the shock front can be obtained, whereby the wave field of HVI-generated shock waves can be depicted in a three-dimensional manner.

2.2. Numerical Implementation

With the developed modeling approach, numerical simulation was implemented on ANSYS®/Autodyn platform. A kernel B-spline weighting function was used as the smoothing function (*i.e.*, W in Eq. (1)), owing to its resemblance to the Gaussian function whereas featuring a narrower compact support compared to the Gaussian function, which reads

291
$$W(R,h)=\frac{3}{2\pi h^3}\times\begin{cases}\frac{2}{3}-R^2+\frac{1}{2}R^3, & (0\le R<1)\\ \frac{1}{6}(2-R)^3, & (1\le R<2)\\ 0. & (R\ge 2)\end{cases} \tag{13}$$

292 In the above, $R=r/h$ (r: the distance between a specific SPH particle and the central
293 particle in Ω; h: the smoothing length of Ω[28]).

294

295 Particularly, for the region of the target structure which is distant from the HVI spot,
296 HVI-induced waves will take the formality of elastic waves guided by the target structure,
297 for which an FE method shows more computationally efficient than the SPH algorithm.
298 That is because, as explained previously, the SPH algorithm searches the updated
299 neighboring particles and creating a new Ω for each particle at every single calculation step,
300 this consuming vast computational cost when compared with an FE algorithm (in FE, the
301 nodes to define an element are remained the same at each calculation step).

302

303 To reap the respective merits that SPH and FE possess, a hybrid modeling, using 3D-SPH
304 to simulate the waves propagating in the vicinity of HVI spot, and using FE for the rest of
305 the target structure, was formulated. To ensure compatibility at the interface between two
306 parts whereas not at the cost of sacrificing numerical stability, coordinates of the SPH
307 particles at the interface were enforced to coincide, via a tie-type bonding condition, with
308 those of their corresponding FE nodes sharing the same spatial locations. In the hybrid
309 modeling, the SPH particle size was 0.2 mm approximately, which was determined to
310 compromise simulation preciseness and computational cost. The default FE element was a
311 3D linear eight-node brick element. For a faithful delineation of wave propagation, ten FE
312 nodes were allocated per wavelength. Previous experiment results [34] under the same
313 impact condition were referenced, so as to estimate the wavelength of shock waves

induced by HVI and accordingly determine the element size, which was circa 0.5 mm in this study. To ensure simulation stability and convergence, the time step in the explicit calculation was set, according to the Courant–Friedrichs–Lewy condition (CFL) condition[28], as

$$\Delta t = \frac{\min(h)}{c}, \tag{14}$$

where $\min(h)$ is the smallest distance between two neighboring SPH particles over Ω, or the smallest interval between two FE nodes; and c the wave propagation velocity within the concerned calculation window.

HVI-induced wave propagation in the target structure was real-time monitored by acquiring in-plane strains of either the SPH particles or FE nodes at the locations where lead zirconate titanate (PZT) wafers were surface-bonded to the target structure in experiment for capturing wave signals. These particles and FE nodes are called "*gauge points*" hereinafter. At gauge points, in-plane (*y*-*z*) strains along wave propagation direction with an angle of θ with regard to *z* axis (referring to **Figure 1**(a)) is expressed as

$$\varepsilon = \varepsilon_z \cos^2\theta + \varepsilon_y \sin^2\theta + 2\varepsilon_{zy} \sin\theta\cos\theta, \tag{15}$$

where ε_z, ε_y and ε_{zy} are the normal strains along *z* axis, along *y* axis and shear strain in *y*-*z* plane, respectively. Both symmetric and anti-symmetric wave modes co-exist in a plate structure upon HVI, and this can be corroborated by Eq. (4): the HVI-induced shock waves (reflected by the pressure) feature two components: the hydrostatic stress ($-p\delta^{\alpha\beta}$) that excites the longitudinal wave modes – the major wave component forming a symmetric wave mode; and the deviatoric stress ($\tau^{\alpha\beta}$) which corresponds to the transverse wave modes – the mode dominating an anti-symmetric wave mode. Considering this, symmetric strains (reflecting symmetric wave modes) and anti-symmetric strains (reflecting

anti-symmetric modes) were respectively extracted from Eq. (15), by summating and subtracting the strains captured at the same in-plane location whereas on two opposite surfaces of the target structure, respectively.

3. Case Studies

With the developed modeling and simulation approach, HVI-induced shock waves were interrogated, with particular emphasis on wave propagation in the vicinity of HVI spot.

3.1. Description of Problem and Modeling

The target structure under consideration was a thin plate 2 mm in its thickness (aluminum 2024), and the projectile was a sphere 3 mm in its diameter (aluminum 1100). Allowing for the geometric symmetry of both the projectile and target structures, half the target plate (measuring 400 mm × 200 mm × 2 mm) and half the sphere projectile were modeled using the hybrid modeling.

Two HVI scenarios – normal and oblique incidence of the projectile (32^0 with regard to the normal direction (x axis) in the symmetric plane, as seen in **Figure 1(a)**) – were respectively considered. The constructed hybrid model is shown in **Figure 1(b)**. The symmetric boundary conditions were applied at the symmetric plane. In the model, the vicinity of HVI spot was defined as 30 mm × 15 mm × 2 mm, the insert of **Figure 1(b)**, which, together with half the sphere projectile, was simulated with 3D-SPH. With the selected particle size (0.2 mm), circa 127,000 SPH particles were created. For the rest of the target structure, approximately 1.2 million FE elements were meshed with a uniform element size of 0.5 mm × 0.5 mm × 0.5 mm.

The key material properties of the projectile and target structures are listed in **Table 1**. The initial impacting velocity of the projectile was 4117 m/s and 4050 m/s, respectively for the normal and oblique cases (in consistent with experiment for comparison purpose). Besides the Shock EOS and Steinberg Guinan strength model adopted in the hybrid modeling, the maximum principal tensile failure stresses for the projectile and target structure were set as 185 MPa and 400 MPa, respectively, which were used as failure thresholds in modeling.

3.2. Normal HVI: Results and Discussion

Simulation for the normal HVI scenario was performed for a duration of 1×10^{-4} *s* since the impact initial. Several snapshots, recording the HVI-produced debris clouds at typical instants within this duration, are exhibited in **Figure 2[35]**, compared with those obtained from experiment [34], to observe good coincidence between simulation and experimental results, including the shape and size of the HVI-generated debris clouds in the front and behind the target structure. Such coincidence has well demonstrated the effectiveness and accuracy of the developed hybrid modeling and simulation approach, setting a basis for subsequent analysis of shock waves.

To facilitate quantitative scrutiny of captured shock wave signals, a compression ratio μ was introduced, to calibrate the degree of material compression due to shock waves. μ, to be linked to the shock wave velocity v_s via Eqs. (7) and (9), is found as

$$\begin{cases} v_s = \dfrac{c_0(1+\mu)}{1-(s-1)\mu}, \\ \mu = \dfrac{\rho_H}{\rho_0} - 1. \end{cases} \tag{16}$$

With Eq. (16), the relationship between the velocity of HVI-induced shock wave and the

385 compression ratio of the target structure is plotted in **Figure 3(a)**, to notice a monotonic
386 increase of the wave propagation velocity as the increase of compression ratio.
387
388 Thirteen gauge points along the wave propagation path from HVI spot were used for signal
389 acquisition in terms of Eq. (15), with respective coordinates in **Table 2**. In the table, the
390 accordingly obtained compression ratios at these gauge points are also listed, revealing a
391 monotonic decrease of compression ratio as radical propagation of shock waves (due to the
392 attenuation of wave energy as propagation). To put it into a perspective, by projecting the
393 compression ratio at the 13 gauge points to **Figure 3(a)**, the relationship between shock
394 wave velocity v_s and propagation distance can be established, shown in **Figure 3(b)**,
395 explicitly implying that v_s reaches 6600 m/s immediately after HVI occurrence, and then
396 drops rapidly to 5300 m/s after propagating a short distance of 8 mm – exactly the velocity
397 of bulk waves in the material of the target structure. This observation reveals that as the
398 shock waves propagate, the HVI-induced pressure drops dramatically as a consequence of
399 the wave attenuation at a rate of the square of propagation distance; subsequently, shock
400 waves convert to the bulk waves and are guided by the plate by taking the formality of
401 Lamb waves - the waves which have been the core of intensive research for developing
402 guided-wave-based damage detection [36-38]. Therefore, in the areas distant from the HVI
403 spot, propagation of the waves can be described using the plate wave theory.
404
405 To further delve into the wave traits, the acquired in-plane strain signals at gauge point (0,
406 42, 42), as an example, together with the isolated symmetric and anti-symmetric modes,
407 are shown in **Figure 4**. It can be noticed that in **Figure 4(b)** the symmetric wave mode (*i.e.*,
408 the first-arrival wave), which is dominated by longitudinal wave components, propagates
409 faster with higher signal magnitude than the anti-symmetric mode in which transverse

wave components prevail. This confirms that the symmetric wave dominates HVI-induced wave energy.

All the captured wave signals were processed with spectrum analysis via Fast Fourier Transform (FFT). Using the signal in **Figure 4** as an example, spectra of the symmetric and anti-symmetric modes are compared in **Figure 5**, revealing distinct signal energy distribution in between. For the former, the wave energy is dispersed in a wider frequency range with majority of it below 1 MHz (upper of **Figure 5**), in comparison with that of the latter which is observed to be concentrated below 200 kHz with a peak value near 30 kHz (lower of **Figure 5**). Notably, such a trait of energy distribution of HVI-induced shock waves can be attributed to the dramatic pressure rise in a transient period during HVI, making the impact as a pulse excitation and distributing symmetric wave energy in a wider band; while on the other hand, the anti-symmetric mode is insensitive to such transient pressure rise, and thus it presents a relatively concentrated energy distribution in a narrower band. Such observation can be interpreted in terms of the governing equation of anti-symmetric modes – the strength model as mentioned earlier – which is not directly related to the pressure as seen in Eq. (11).

Taking a step further, the time-frequency spectrographic analysis via wavelet transform (WT) was applied on captured signals. **Figure 6** exemplarily shows the WT spectrographs of the signals in **Figure 4**, integrated with the group velocity dispersion curve theoretically obtained for comparison purpose. It is explicit that HVI excites higher-order symmetric modes, **Figure 6(a)**, including S_1 and S_2, on top of the fundamental S_0; whereas this is not the case for anti-symmetric modes as only the fundamental anti-symmetric mode (A_0) is prominent in the spectrograph as seen in **Figure 6(b)**.

436 Using the hybrid model, displayed in **Figure 7** is the progressive changes in material
437 attributes in the vicinity of HVI at several instants upon HVI, highlighting distribution of
438 the elastic, plastic, as well the failure regions. In the model, the strength model and failure
439 criteria served as the governing rules to judge the material attributes. As observed, in a
440 duration of about 1.2×10^{-6} s from the commencement of HVI, the plastic region, which is
441 larger than the projectile size, is initiated at a faster speed than that of the formation of the
442 failure region, and then the plastic region fails when the maximum principal stress exceeds
443 the defined values in the failure criteria. In the plastic region, the material presents
444 fluid-like properties and loses part of its shear strength. Crack-like failures are produced at
445 the perimeter of the plastic region, as seen in **Figure 7**, which represent the cracks at the
446 edge of crater or orifices induced by HVI in reality or experiment. Conclusively, an HVI
447 exerts a larger influence area compared to the geometric size of the projectile.
448
449 **3.3. Oblique HVI: Results and Discussion**
450 Realistically, a projectile impacts a target structure in an oblique instead of a normal
451 direction. Using the hybrid modeling and the same signal analysis procedures, the oblique
452 HVI is reflected by representative snapshots of produced debris clouds displayed in
453
454
455
456
457
458
459 **Experiment**

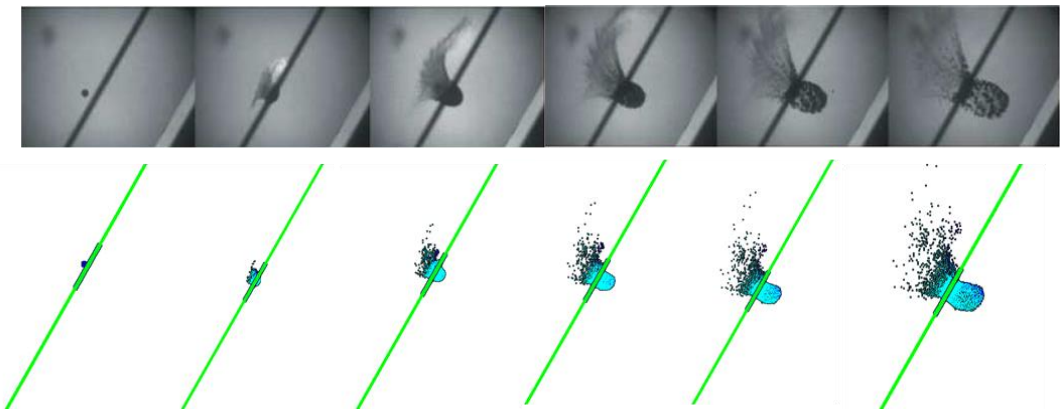

Simulation

Figure 8. Compared with those captured at corresponding moments in experiment [34], it shows a qualitative coincidence in between.

As a counterpart of **Figure 7** (for normal HVI), **Figure 9** presents the progressive changes in material properties in the vicinity of HVI in the oblique case, provided the same strength model and failure criteria adopted. It can be seen that in **Figure 9** the ultimate failure region takes an elliptic shape and is surrounded by distributed failure points scattered in the region.

3.4. Anisotropy of Shock Wave Propagation

Distinct from a normal HVI, an oblique HVI introduces prominent anisotropy in wave propagation, as evidenced by certain discrepancy in wave velocity and dispersive natures in different propagation directions. This might downgrade the accuracy of an AE-based damage localization exercise, if the three basic hypotheses mentioned earlier remain for

developing localization algorithm (*i.e.*, the velocity of HVI-induced wave is constant, the wave mode is haploid, and wave dispersion can be ignored).

Figure 10 shows the shock wave signals acquired at the same propagation distance of 30 mm from the HVI spot whereas at different propagation directions (0°, 30^0, 45^0, 60^0, 90^0, 120^0, 135^0, 150^0 and 180^0 with regard to *z*-axis), under the normal and oblique cases, respectively. For normal HVI, **Figure 10(a)**, no discernible discrepancy in both the arrival time and magnitude of the first-arrival wave component can be seen among the signals captured at different angles. The very slight difference among signals, as seen in **Figure 10(a)**, lies on the fact that the model, discretized into the lattice using evenly distributed SPH particles, is not strictly a centrosymmetric meshing. However, the sequent wave components following the first-arrival wave (comprising reflections from boundaries) tend to have increasing divergence.

For the oblique HVI, the anisotropy of wave propagation becomes prominent. Using the gauge point 30 mm from HVI spot as an example (**Figure 10 (b)**), the difference in arrival time between waves at 0^0 and 180^0 increases from 0.09 *us* in normal HVI to 0.19 *us* in this oblique case, this resulting in an error of circa 1 mm in the spatial domain with the calculated shock wave propagation velocity.

However, it is noteworthy that although the oblique HVI introduces anisotropy in wave propagation, its overall influence on the first-arrival wave component is minute with neglectable impact on AE-based HVI localization (as demonstrated in the above, the spatial error is 1 mm only); but it is not the case for the signal magnitude as the magnitude decreases monotonically as the angle increases from 0^0 to 180^0, this requesting appropriate compensation if the signal magnitude is also a factor to be exploited for HVI localization.

4. Localization of HVI Spot

Based on the understanding of propagation characteristics of HVI-induced shock waves, an AE-based characterization strategy for HVI-committed damage was developed, in conjunction with the use of an enhanced delay-and-sum-based diagnostic imaging algorithm. Observing **Figure 4-6**, it is relevant to note that a symmetric mode, compared with its anti-symmetric counterpart, features a much less dispersive nature with a larger signal magnitude, making it a good candidate to serve the purpose of localization of HVI.

4.1. Algorithm

Without loss of the generality, one can assume HVI spot is at (y, z) on the target structure which is surface-affixed with a sparse sensor network consisting of N PZT wafers. The first-arrival wave captured by the i^{th} sensor located at (y_i, z_i) (denoted with P_i) can be expressed as

$$t_i = t_0 + t_{shock-i} + \Delta t_i \,, \tag{17}$$

where t_0 is the time moment when the projectile impacts the target structure; $t_{shock-i}$ the propagation time of HVI-induced S_0 propagating from the HVI spot to the perimeter of the area within which the material is extremely and transiently compressed due to HVI so that it behaves plastically (this area is termed "***HVI-influenced area***" hereinafter); Δt_i the subsequent traveling time for S_0 from the perimeter of the HVI-influenced area to P_i.

Taking another PZT wafer in the sparse sensor network into account, say P_j at (y_j, z_j), the time difference (Δt) in the arrival time of S_0 (*i.e.*, the first-arrival wave mode in the signal) from the HVI spot to P_i and from the spot to P_j yields

$$\Delta t = t_i - t_j = (t_0 + t_{shock-i} + \Delta t_i) - (t_0 + t_{shock-j} + \Delta t_j)$$
$$= \frac{(\Delta d_i - \Delta d_j)}{v_{plate}} + \int \frac{dr_i}{v_{HVI-i}} - \int \frac{dr_j}{v_{HVI-j}} \tag{18}$$
$$= \frac{(\sqrt{(y-y_i)^2 + (z-z_i)^2} - r_i) - (\sqrt{(y-y_j)^2 + (z-z_j)^2} - r_j)}{v_{plate}} + \int_0^{r_i} \frac{dr_i}{v_{HVI-i}} - \int_0^{r_j} \frac{dr_j}{v_{HVI-j}}.$$

Variables in Eq. (18) are discriminated by subscripts i and j for two PZT wafers. For P_i, Δd_i is the distance for S_0 propagating from the perimeter of HVI-influenced area to P_i; r_i signifies the distance for the same wave mode traveling from HVI spot to P_i within the HVI-influenced area; v_{plate} is the velocity of S_0 outside the HVI-influenced area (*i.e.*, in the elastic region); v_{HVI-i} denotes the velocity of shock wave in the HVI-influenced area (*i.e.*, in the plastic region), and it varies along wave propagation, which has been ascertained from the hybrid modeling, displayed in **Figure 3**.

In a normal HVI scenario, it is straightforward that $r_i = r_j$; for an oblique incidence, given that the maximum error in the spatial domain along different wave propagation directions (*i.e.*, taking wave propagation anisotropy into account) is less than 1 mm, one has $r_i \approx r_j$. This means the error due to the difference in wave propagation in the elastic and plastic regions could be minute, for the purpose of HVI localization. Thus, for both scenarios, Eq. (18) can be simplified as

$$\Delta t = t_i - t_j \approx \frac{(\sqrt{(y-y_i)^2 + (z-z_i)^2}) - (\sqrt{(y-y_j)^2 + (z-z_j)^2})}{v_{plate}}. \tag{19}$$

Mathematically, Eq. (19) describes a locus of roots, and the difference between distances from any point on the locus to two sensors is a constant, *i.e.*, a hyperbola with P_i and P_j being its two foci. Using a diagnostic imaging approach residing on *delay-and-sum* principle [39], each sensor pair in the sensor network creates a two-dimensional binary gray-scale synthetic image, in which a pixel is linked to the probability of HVI spot therein

– a perception as to the existence of HVI spot from the sensor pair that creates such an image. In Eq. (19), only v_{plate} is associated with material properties, and thus the degree of negative impact on localization accuracy, from the inhomogeneity or uncertainties in materials, is expected to be ignorable, endowing the algorithm with error tolerance to a certain degree.

Eq. (19) also indicates that all the pixels in the image which produce the same Δt locate on a set of hyperbola. A set of hyperbola suggests possible locations of HVI spot - the perceptions as to the HVI event from the perspective of the sensing group (P_i and P_j) that creates such a hyperbola. In principle, the pixels right on the locus have the highest degree of probability (100%) as to the presence of HVI, and for other pixels, the greater the distance to the locus the lower the probability that HVI-induced damage exists therein. Such a probability is calibrated in terms of gray-scale. Quantitative depiction of HVI-induced damage can further be achieved by locally canvassing those pixels with singularly elevated values. Aggregating the images rendered by all sensing pairs in the sensor network yields a superimposed image (*ultimate resulting image* in what follows) - a collective consensus as to HVI from the entire sensor network.

4.2. Results and Discussion

Displayed in **Figure 11 (a)** is an ultimate resulting image constructed with four PZT sensors randomly placed at (0, 0, 150), (0, -127, 127), (0, -120, 0) and (0, 180, 0), in which a multitude of pseudo-spot near the real spot, along with increased noise interference, can be observed. To mitigate the influence of noise interference and in the meantime minimize pseudo-spots, the subsequent wave components (including higher-order symmetric modes, fundamental anti-symmetric mode, and multiple reflections from boundaries of the target

structure) pursuant to the first-arrival S_0 were screened. The accordingly constructed ultimate resulting images for both normal and oblique HVIs are presented in **Figure 11 (b) and (c)**. For the normal scenario, using the same four sensors as shown in **Figure 11 (b)**, an improved identification precision in comparison with results in **Figure 11 (a)**, in which no screening process was applied, is shown. Similarly, the accurate resulting image for the oblique HVI scenario is shown in **Figure 11 (c)**.

The proposed HVI localization algorithm has provided a potential for real-time monitoring of HVI and orbital debris-produced damage in space structures. During practical implementation, a multitude of sensors will be used to configure a sensor network, to address sufficient redundancy in signal acquisition, whereby the mal-function of particular sensors (for example failure of a sensor due to HVI) would not cause significant reduction in monitoring results.

5. Concluding Remarks

HVI has been the subject of intensive scrutiny over the years as a result of the burgeoning development of human activities in outer space. Different from LVI, HVI features transient, localized, and extreme material deformation, under which the induced shock waves present unique yet complex features. In recognition of the lack in the fundamental know-how on propagation of HVI-induced shock waves, a dedicated modeling and numerical simulation approach was developed, based on the three-dimensional smooth-particle hydrodynamics (SPH) in conjunction with the finite element method, whereby both normal and oblique HVI cases were interrogated quantitatively, showing good coincidence with experimental results. The obtained results have revealed that an HVI event induces a dramatic pressure rise in a transient time instant, leading to shock waves which attenuate at a rate of the

square of propagation distance, until the waves convert to bulk waves guided by target structures in the regions distant from the HVI spot. Spectrum analyses underscored that multiple wave modes co-exist in the induced shock waves, with energy dominated by the symmetric modes and dispersed in a wide frequency range with majority of it below 1 MHz, along with minor energy carried by the anti-symmetric modes below 200 kHz with a peak value near 30 kHz. All these observations are significantly different from waves in LVI. An oblique HVI introduces prominent anisotropic attributes in wave propagation. Nevertheless, due to the high velocity of the shock waves, the overall influence on the first-arrival wave component is minute, impacting neglectable influence on AE-based localization of HVI spot; but it is not the case for signal magnitude, entailing appropriate compensation if the signal magnitude is also a factor to be exploited for spot localization. This conclusion has been demonstrated using an AE-based localization exercise for HVI spot in simulation, in which the developed localization algorithm, based on understanding of the HVI-induced shock waves and an enhanced delay-and-sum-based diagnostic imaging algorithm, precisely located HVI spots in both normal and oblique cases. Last but not the least, it is expected that in a real HVI experiment, a wide range of factors, including material inhomogeneity and measurement noise or uncertainties, could downgrade the accuracy of the proposed localization algorithm, to be canvassed in an upcoming study.

Acknowledgments

This project is supported by the Hong Kong Research Grants Council via General Research Funds (No. 523313 and No. 15214414).

References

[1] Mihaly, J. M., Tandy, J. D., Rosakis, A. J., Adams, M. A., and Pullin, D., 2014, "Pressure-Dependent, Infrared-Emitting Phenomenon in Hypervelocity Impact," Journal of Applied Mechanics, 82(1), p. 011004.

[2] Li, Y. Q., Li, X. G., and Gao, X. L., 2015, "Modeling of Advanced Combat Helmet Under Ballistic Impact," Journal of Applied Mechanics, 82(11), p. 111004.

[3] Nicholas, T., 2008, "Introduction: High Velocity Impact," AIAA Journal, 46(2), pp. 289-289.

[4] Ramjaun, D., Kato, I., Takayama, K., and Jagadeesh, G., 2003, "Hypervelocity impacts on thin metallic and composite space debris bumper shields," AIAA journal, 41(8), pp. 1564-1572.

[5] Razzaqi, S. A., and Smart, M. K., 2011, "Hypervelocity Experiments on Oxygen Enrichment in a Hydrogen-Fueled Scramjet," AIAA journal, 49(7), pp. 1488-1497.

[6] Murr, L. E., Quinones, S. A., Ferreyra, T. E., Ayala, A., Valerio, O. L., Hörz, F., and Bernhard, R. P., 1998, "The low-velocity-to-hypervelocity penetration transition for impact craters in metal targets," Materials Science and Engineering: A, 256(1–2), pp. 166-182.

[7] WG3, I., 2013, "Sensor Systems to Detect Impacts on Spacecraft."

[8] Wright, D., 2009, "Colliding Satellites: Consequences and Implications," Union of Concerned Scientists, 26.

[9] Christiansen, E. L., 1993, "Design and performance equations for advanced meteoroid and debris shields," International Journal of Impact Engineering, 14(1), pp. 145-156.

[10] Cour-Palais, B. G., and Crews, J. L., 1990, "A multi-shock concept for spacecraft shielding," International Journal of Impact Engineering, 10(1), pp. 135-146.

[11] Drolshagen, G., 2008, "Impact effects from small size meteoroids and space debris," Advances in Space Research, 41(7), pp. 1123-1131.

[12] Kundu, T., Das, S., Martin, S. A., and Jata, K. V., 2008, "Locating point of impact in anisotropic fiber reinforced composite plates," Ultrasonics, 48(3), pp. 193-201.

[13] Coverley, P. T., and Staszewski, W. J., 2003, "Impact damage location in composite structures using optimized sensor triangulation procedure," Smart Materials and Structures, 12(5), pp. 795-803.

[14] He, T., Pan, Q., Liu, Y. G., Liu, X. D., and Hu, D. Y., 2012, "Near-field beamforming analysis for acoustic emission source localization," Ultrasonics, 52(5), pp. 587-592.

[15] Giurgiutiu, V., and Bao, J., 2004, "Embedded-ultrasonics structural radar for in situ structural health monitoring of thin-wall structures," Structural Health Monitoring, 3(2), pp. 121-140.

[16] Raghavan, A., and Cesnik, C. E., 2007, "Review of guided-wave structural health monitoring," Shock and Vibration Digest, 39(2), pp. 91-116.

[17] Prosser, W. H., Gorman, M. R., and Humes, D. H., 1999, "Acoustic emission signals in thin plates produced by impact damage," Journal of Acoustic Emission, 17, pp. 29-36.

[18] Perkins, S., 2010, "Hypervelocity Impact Detection: An Investigation into Piezoelectric Response of PVDF Films," School of Physical Sciences, University of Kent.

[19] Schäfer, F., and Janovsky, R., 2007, "Impact sensor network for detection of hypervelocity impacts on spacecraft," Acta Astronautica, 61(10), pp. 901-911.

[20] Benson, D. J., 1992, "Computational methods in Lagrangian and Eulerian hydrocodes," Computer methods in Applied mechanics and Engineering, 99(2), pp. 235-394.

[21] Ganzenmüller, G. C., Hiermaier, S., and May, M., 2015, "On the similarity of meshless discretizations of Peridynamics and Smooth-Particle Hydrodynamics,"

671 Computers & Structures, 150(0), pp. 71-78.
672 [22] Cherniaev, A., and Telichev, I., 2015, "Meso-scale modeling of hypervelocity impact
673 damage in composite laminates," Composites Part B: Engineering, 74(0), pp. 95-103.
674 [23] Mahmadi, K., and Aquelet, N., 2014, "Euler–Lagrange simulation of high pressure
675 shock waves," Wave Motion, pp. 28-42.
676 [24] Gingold, R. A., and Monaghan, J. J., 1977, "Smoothed particle hydrodynamics-theory
677 and application to non-spherical stars," Monthly Notices of the Royal Astronomical
678 Society, 181, pp. 375-389.
679 [25] Ryan, S., Schäfer, F., Guyot, M., Hiermaier, S., and Lambert, M., 2008,
680 "Characterizing the transient response of CFRP/Al HC spacecraft structures induced by
681 space debris impact at hypervelocity," International Journal of Impact Engineering, 35(12),
682 pp. 1756-1763.
683 [26] Clegg, R., White, D., Riedel, W., and Harwick, W., 2006, "Hypervelocity impact
684 damage prediction in composites: Part I—material model and characterisation,"
685 International journal of impact engineering, 33(1), pp. 190-200.
686 [27] Zhang, Q. M., Long, R. R., Huang, F. L., Chen, L., and Fu, Y. S., 2008, "A model for
687 debris clouds produced by impact of hypervelocity projectiles on multiplate structures,"
688 Applied Physics Letters, 93(21), p. 211905.
689 [28] Liu, M. B., and Liu, G. R., 2010, "Smoothed particle hydrodynamics (SPH): an
690 overview and recent developments," Archives of computational methods in engineering,
691 17(1), pp. 25-76.
692 [29] Anderson, J. D., and Wendt, J., 1995, Computational fluid dynamics, Springer, Berlin.
693 [30] Birdsall, C. K., and Langdon, A. B., 2004, Plasma physics via computer simulation,
694 CRC Press, Boca Raton.
695 [31] Libersky, L. D., Petschek, A. G., Carney, T. C., Hipp, J. R., and Allahdadi, F. A., 1993,
696 "High Strain Lagrangian Hydrodynamics: A Three-Dimensional SPH Code for Dynamic
697 Material Response," Journal of Computational Physics, 109(1), pp. 67-75.
698 [32] Ahrens, T., 1993, "Equation of state," High-Pressure Shock Compression of Solids,
699 Springer, pp. 75-113.
700 [33] Steinberg, D., Cochran, S., and Guinan, M., 2008, "A constitutive model for metals
701 applicable at high‐strain rate," Journal of Applied Physics, 51(3), pp. 1498-1504.
702 [34] Plassard, F., Mespoulet, J., and Hereil, P., 2011, "Hypervelocity impact of aluminium
703 sphere against aluminium plate : experiment and LS-DYNA correlation," Proc. 8th
704 European LS-DYNA Conference.
705 [35] Liu, M., SU, Z., and Yuan, S., 2014, "On propagation characteristics of shock waves
706 generated under hypervelocity impact," Proc. 2nd International Conference of Structural
707 Health Monitoring and Integrity Management CRC Press, pp. 445-450.
708 [36] Sohn, H., and Lee, S. J., 2010, "Lamb wave tuning curve calibration for
709 surface-bonded piezoelectric transducers," Smart Materials and Structures, 19(1), p.
710 015007.
711 [37] Croxford, A. J., Moll, J., Wilcox, P. D., and Michaels, J. E., 2010, "Efficient
712 temperature compensation strategies for guided wave structural health monitoring,"
713 Ultrasonics, 50(4), pp. 517-528.
714 [38] Michaels, J. E., and Michaels, T. E., 2007, "Guided wave signal processing and image
715 fusion for in situ damage localization in plates," Wave Motion, 44(6), pp. 482-492.
716 [39] Wang, C. H., Rose, J. T., and Chang, F.-K., 2004, "A synthetic time-reversal imaging
717 method for structural health monitoring," Smart materials and structures, 13(2), p. 415.
718
719

720

721

722

723 **Table 1.** Material parameters of projectile and target structures

724

AL 1100 (projectile)	ρ_0 (g/cm^3)	Γ	c_0 (m/s)	s	T_0 (K)
	2.707	1.97	5386	1.339	300
	C_v (J/kgK)	G_0 (GPa)	Y_0 (MPa)	Y_{max} (MPa)	Θ
	884	27.1	40	480	400
	n	$\overline{G_p}$	$\overline{G_T}$ (MPa/K)	$\overline{Y_p}$	T_{melt} (K)
	0.27	1.767	-16.69	0.002608	1220
AL 2024 (target)	ρ_0 (g/cm^3)	Γ	c_0 (m/s)	s	T_0 (K)
	2.785	2	5382	1.338	300
	C_v (J/kgK)	G_0 (GPa)	Y_0 (MPa)	Y_{max} (MPa)	Θ
	863	28.6	260	760	310
	n	$\overline{G_p}$	$\overline{G_T}$ (MPa/K)	$\overline{Y_p}$	T_{melt} (K)
	0.185	1.8647	-17.62	0.01695	1220

725

726

727

728

729 **Table 2.** Coordinates and compression ratio of selected gauge points

730

Gauge point number	Coordinates	Compression ratio
1	(0, 1.91, 0)	0.1641
2	(0, 3.93, 0)	0.01355
3	(0, 5.94, 0)	0.00255
4	(0, 7.95, 0)	0.00089
5	(0, 9.97, 0)	0.00073
6	(0, 12, 0)	0.00053
7	(0, 14, 0)	0.00041
8	(0, 30, 0)	0.00029
9	(0, 60, 0)	0.00017
10	(0, 90, 0)	0.00012
11	(0, 120, 0)	0.00009
12	(0, 150, 0)	0.00008
13	(0, 180, 0)	0.00007

731

732

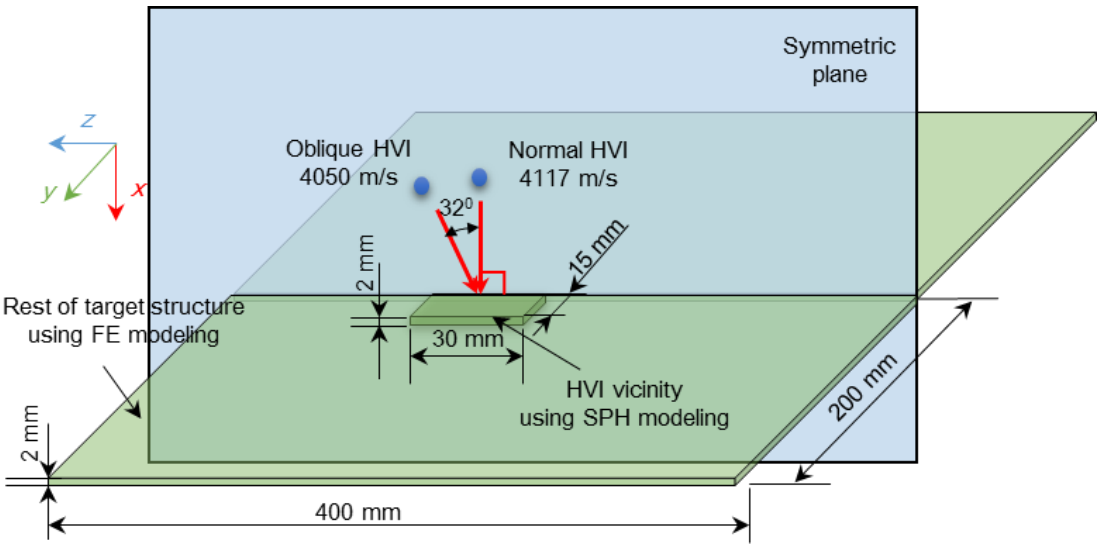
Symmetric
plane
z
y
x
Oblique HVI
4050 m/s
Normal HVI
4117 m/s
32⁰
2 mm
15 mm
Rest of target structure
using FE modeling
30 mm
HVI vicinity
using SPH modeling
200 mm
2 mm
400 mm

(a)

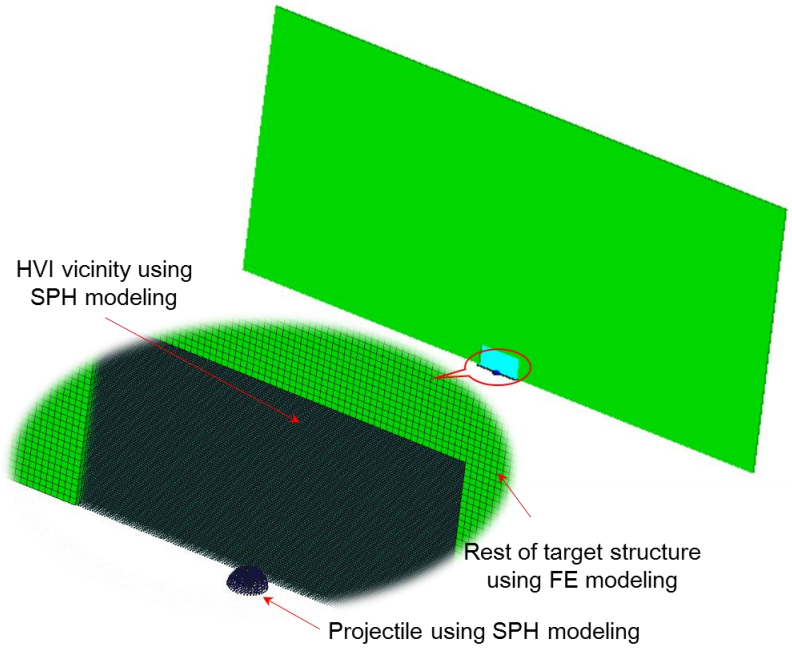

(b)

Figure 1 (a) Sketch of normal and oblique HVI scenarios; and (b) hybrid model showing HVI vicinity (using SPH) and rest of target structure (using FE)

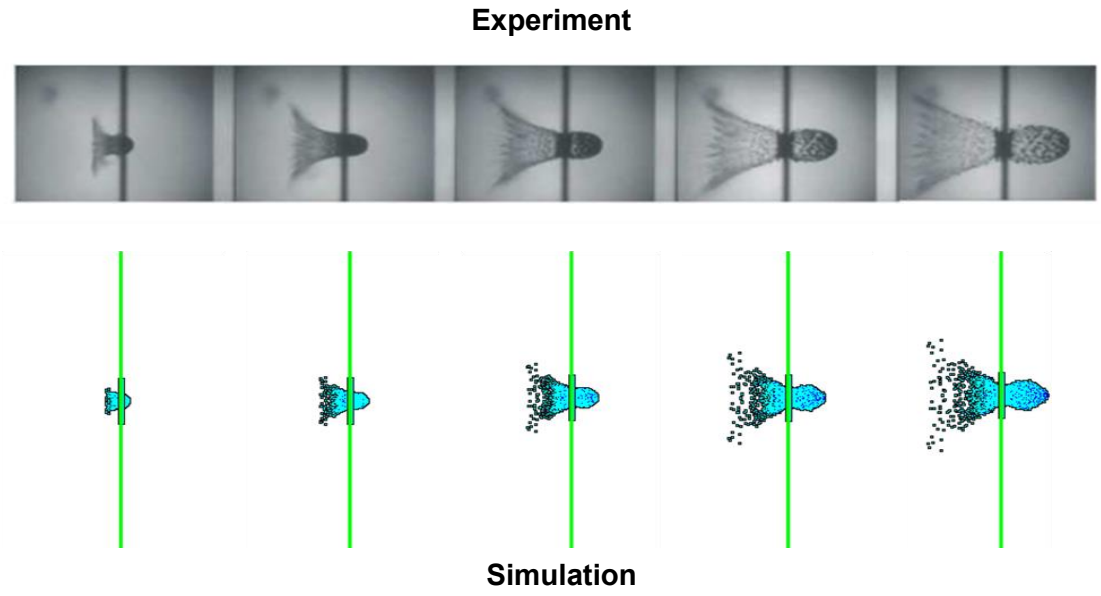

Figure 2 Comparison of simulation and experiment results in normal HVI (frame interval: 2 μs)[35]

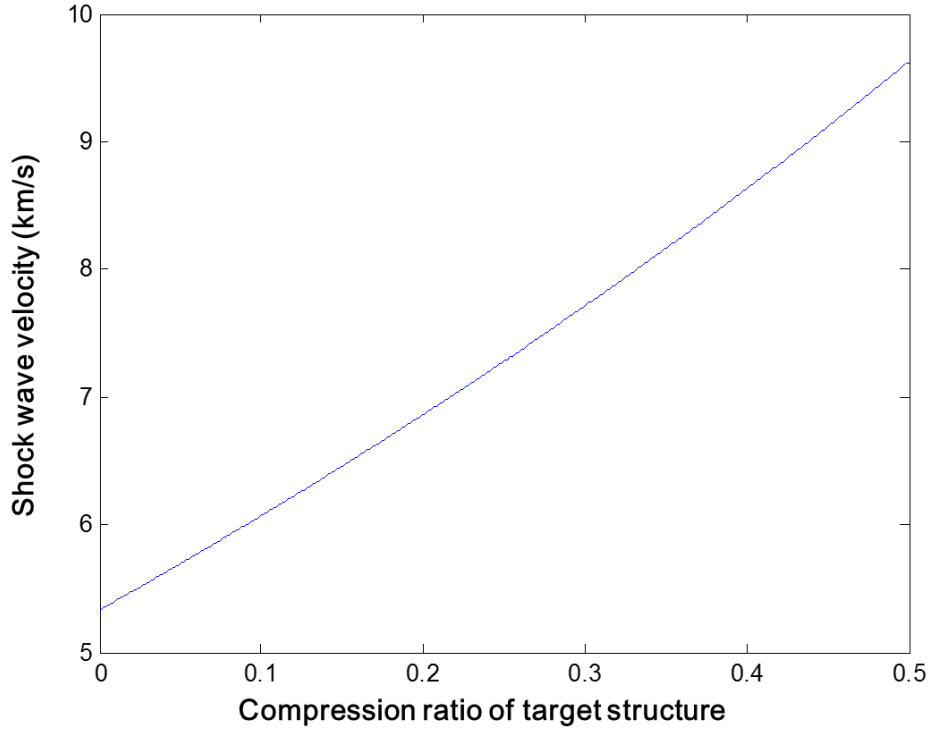

(a)

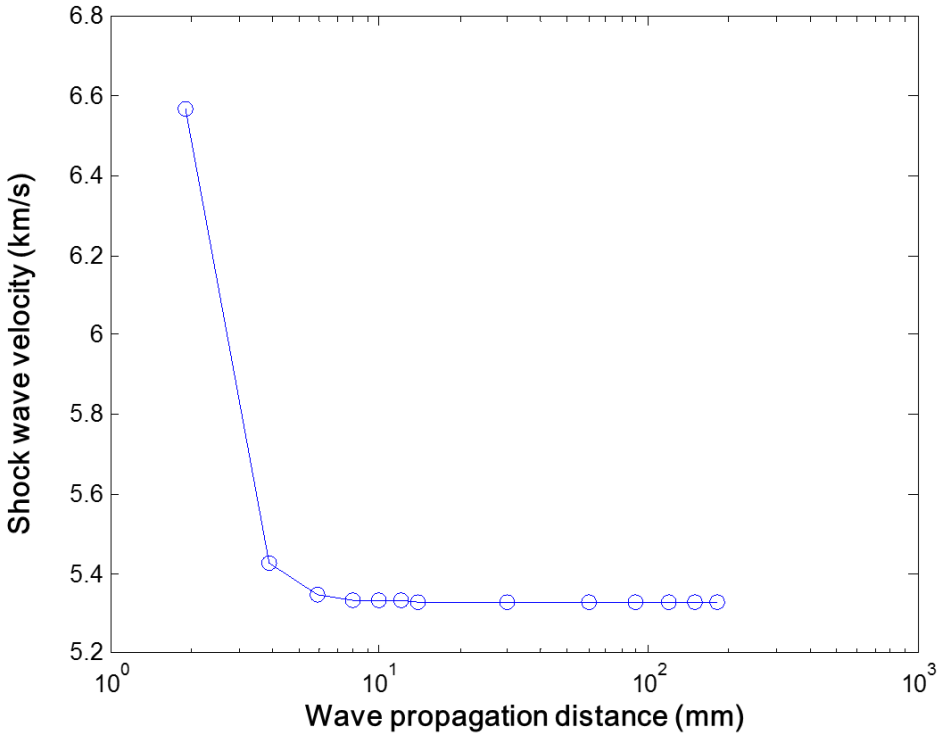

(b)

Figure 3 (a) Relationship between shock wave velocity and compression ratio of target structure obtained using hybrid modeling (b) shock wave velocity *vs.* shock wave propagation distance

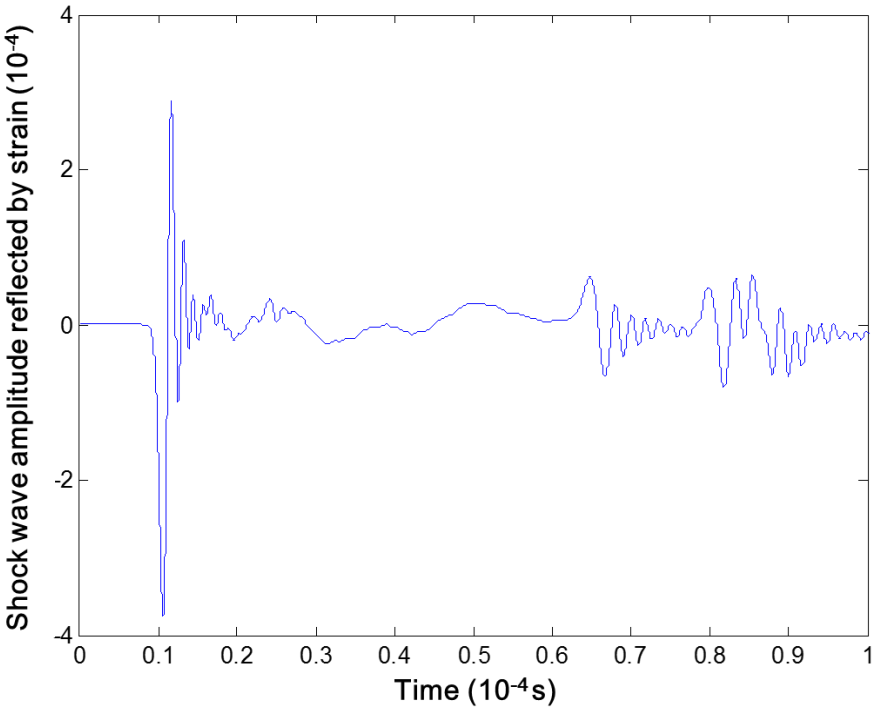

(a)

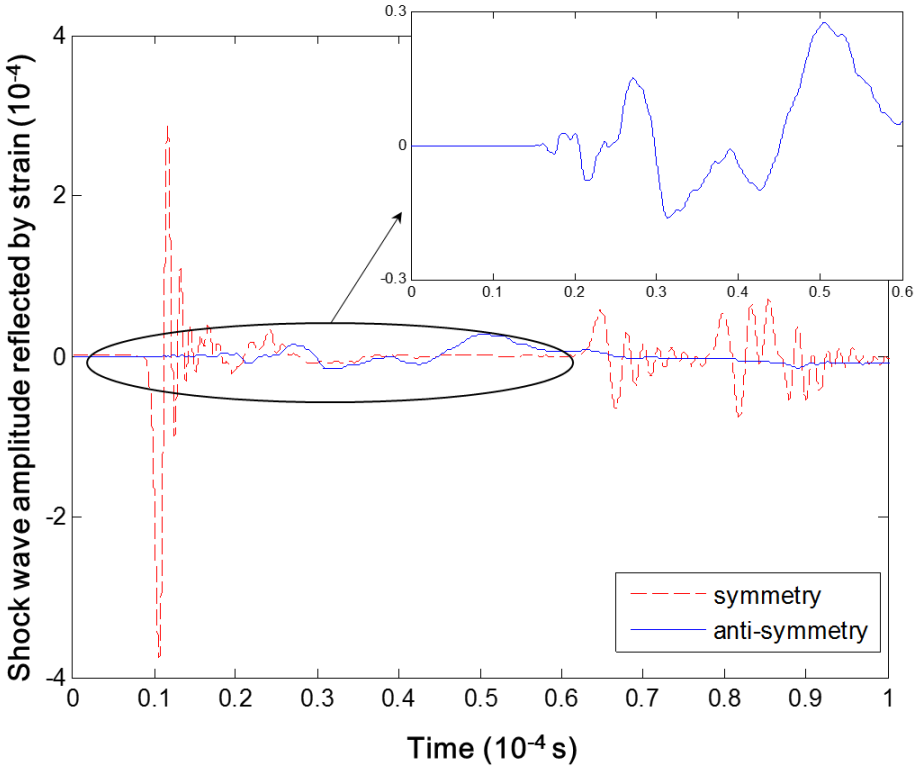

(b)

Figure 4 In-plane strain acquired at gauge point (0, 42, 42) in normal HVI: (a) original signal; (b) isolated symmetric and anti-symmetric mode

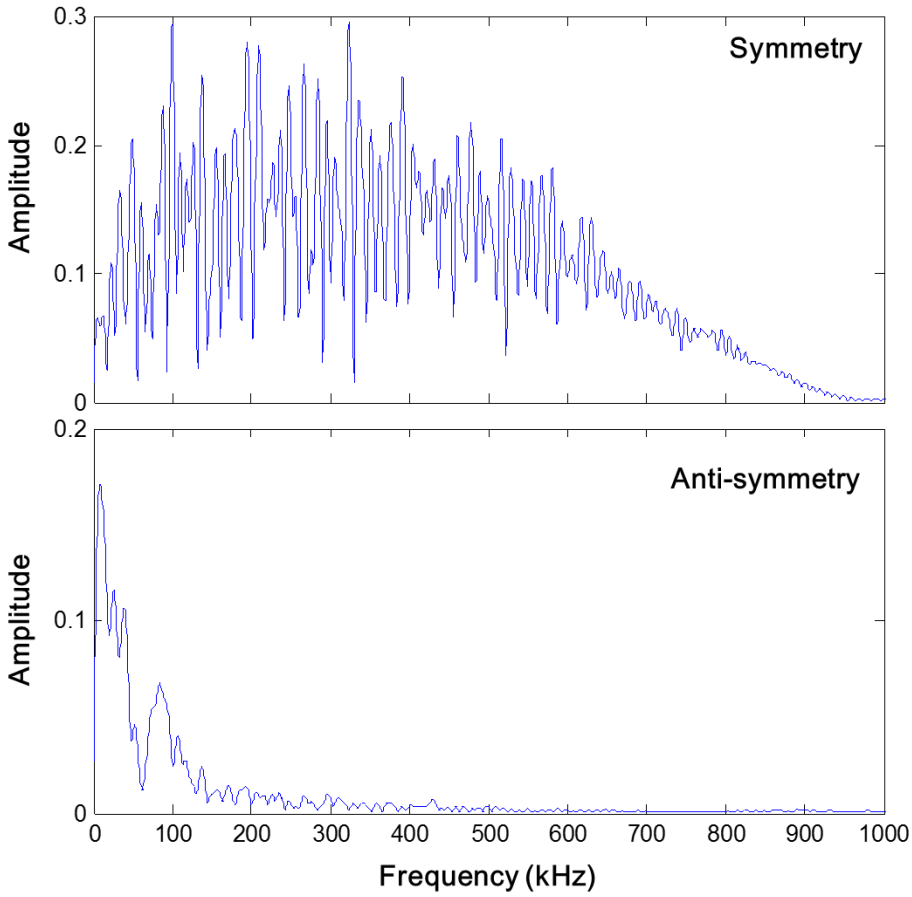

Figure 5 Frequency spectra of in-plane symmetric and anti-symmetric strains in Figure 4

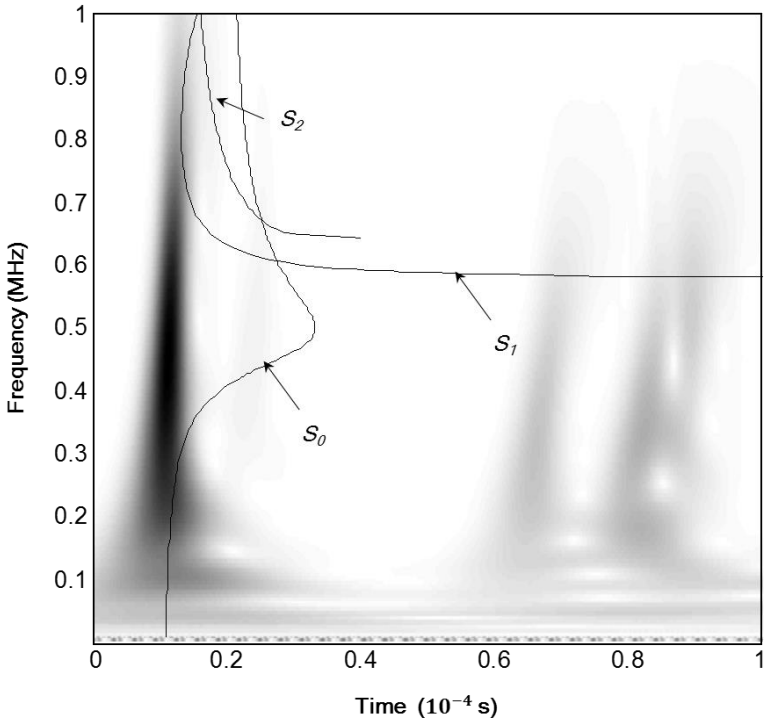

(a)

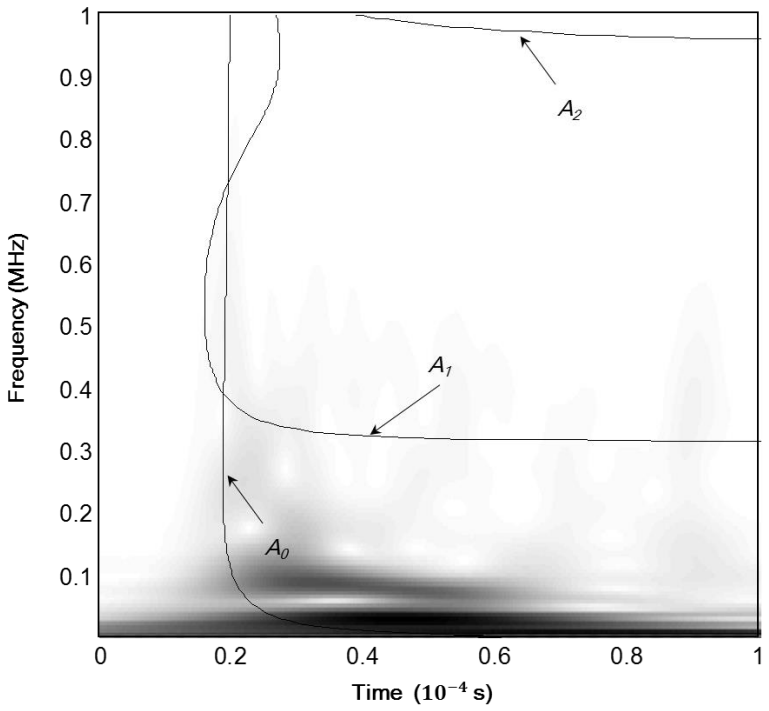

(b)

Figure 6 Wavelet spectrographs of in-plane strain in Figure 4: (a) symmetric mode; and (b) anti-symmetric mode

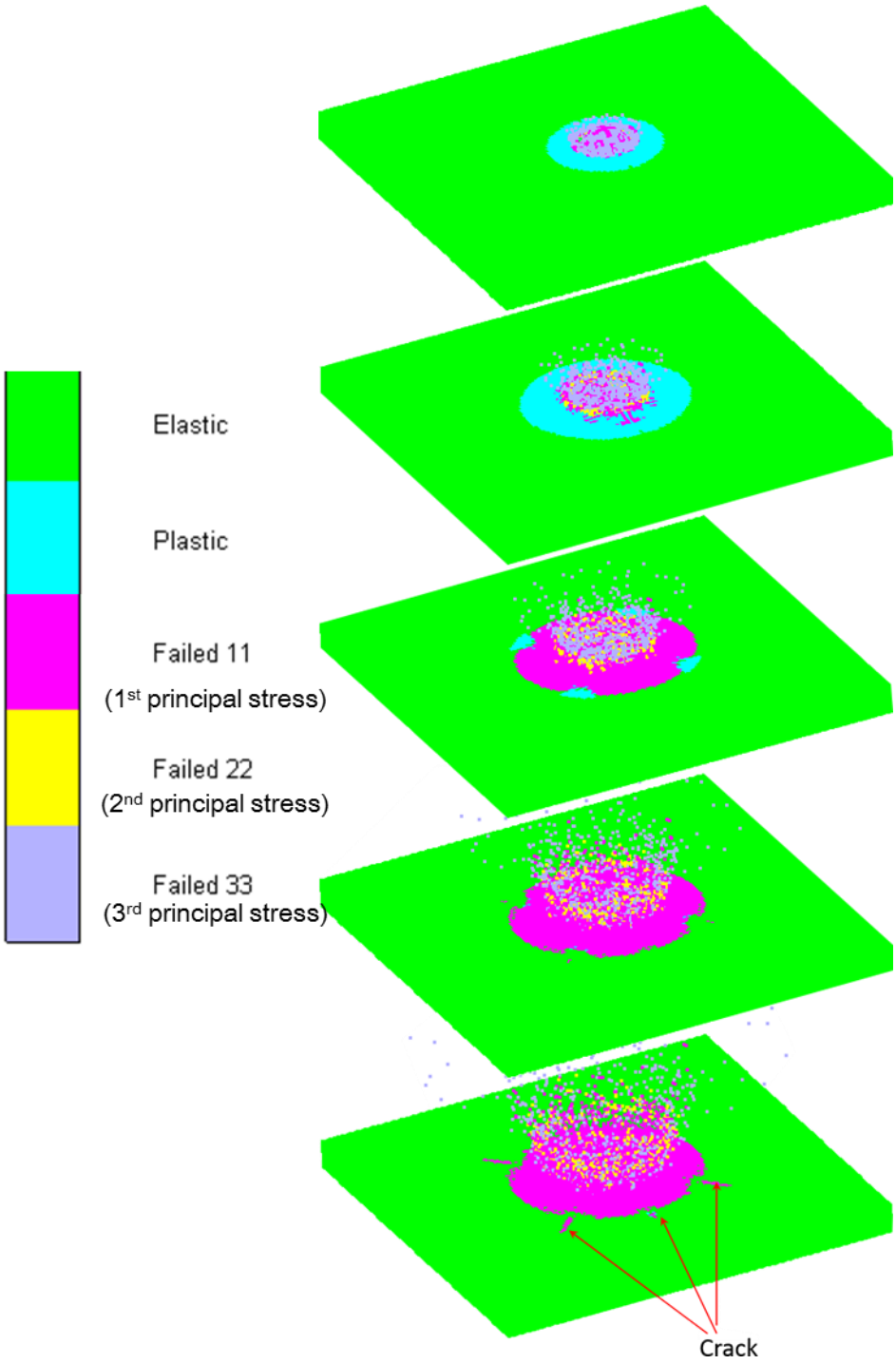

815

816

817

818

819 **Figure 7** Progressive change in material properties in normal HVI at typical instants: 0.4×10^{-6} s,
820 0.8×10^{-6} s, 1.2×10^{-6} s, 2.0×10^{-6} s and 2.8×10^{-6} s

821

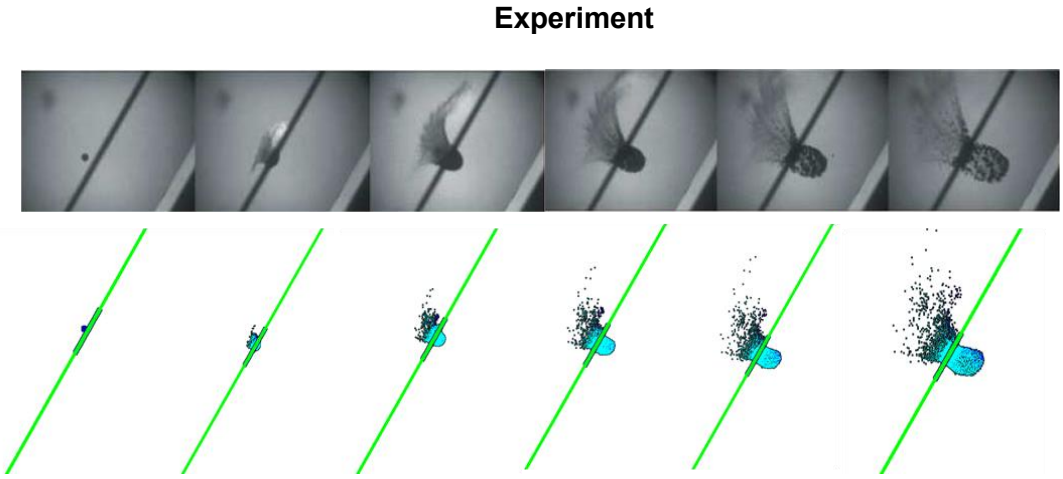

Figure 8 Comparison of simulation and experiment results in oblique HVI (frame interval: 2 μs)

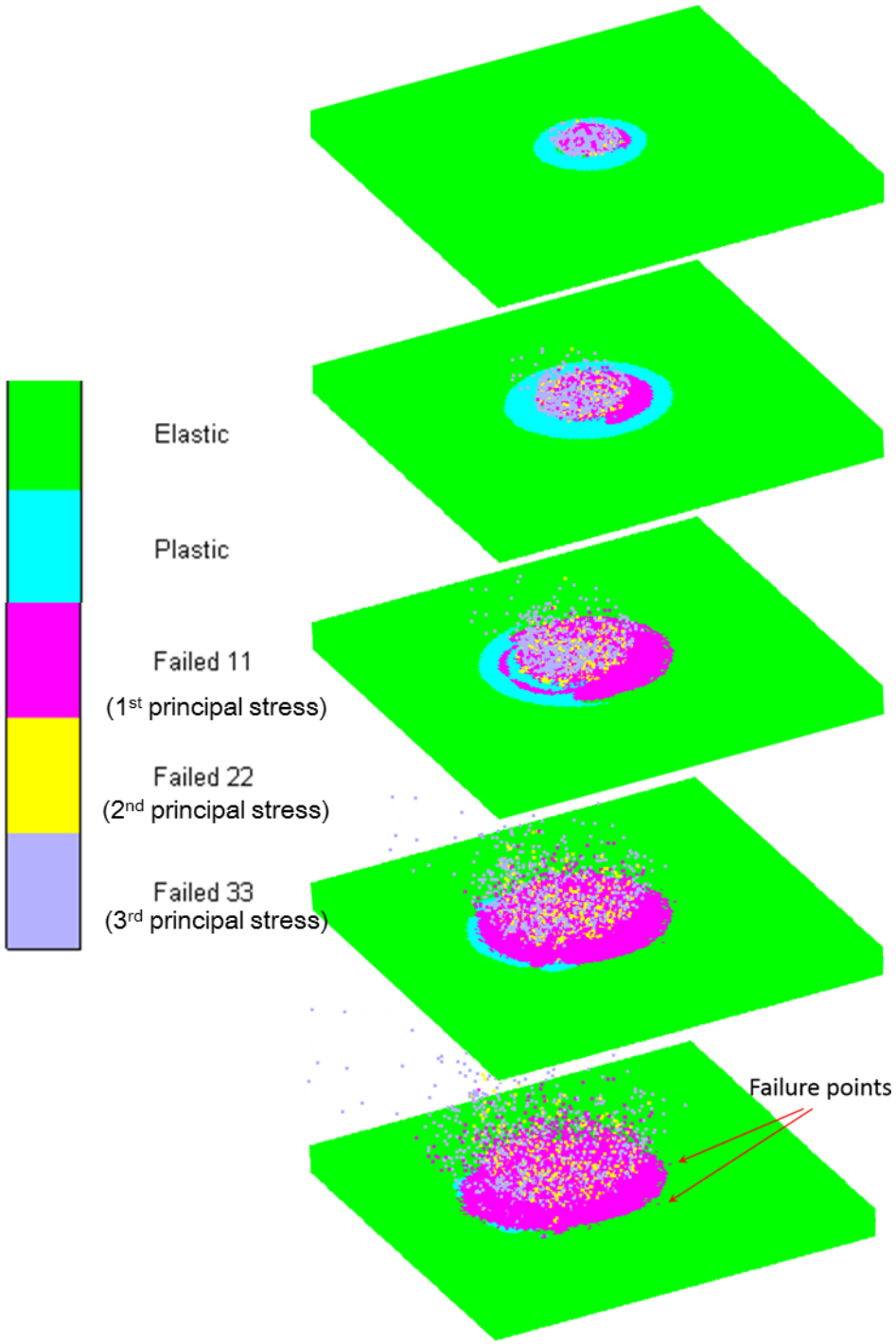

839

840

841

842 **Figure 9** Progressive change in material properties in oblique HVI at typical instants: 0.4×10^{-6} s,
843 0.8×10^{-6} s, 1.2×10^{-6} s, 2.0×10^{-6} s and 2.8×10^{-6} s

844

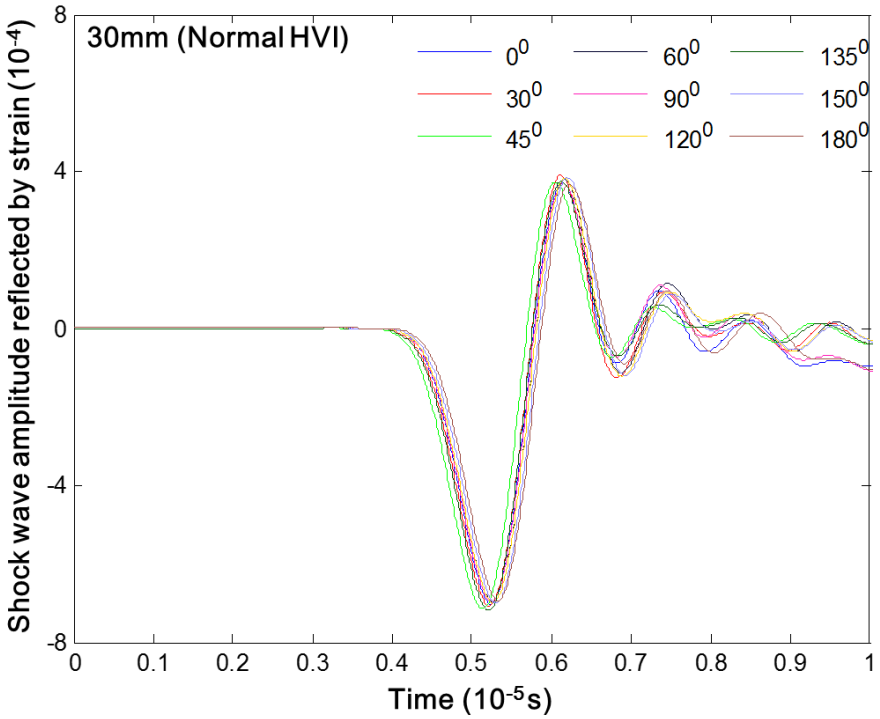

845

846 (a)

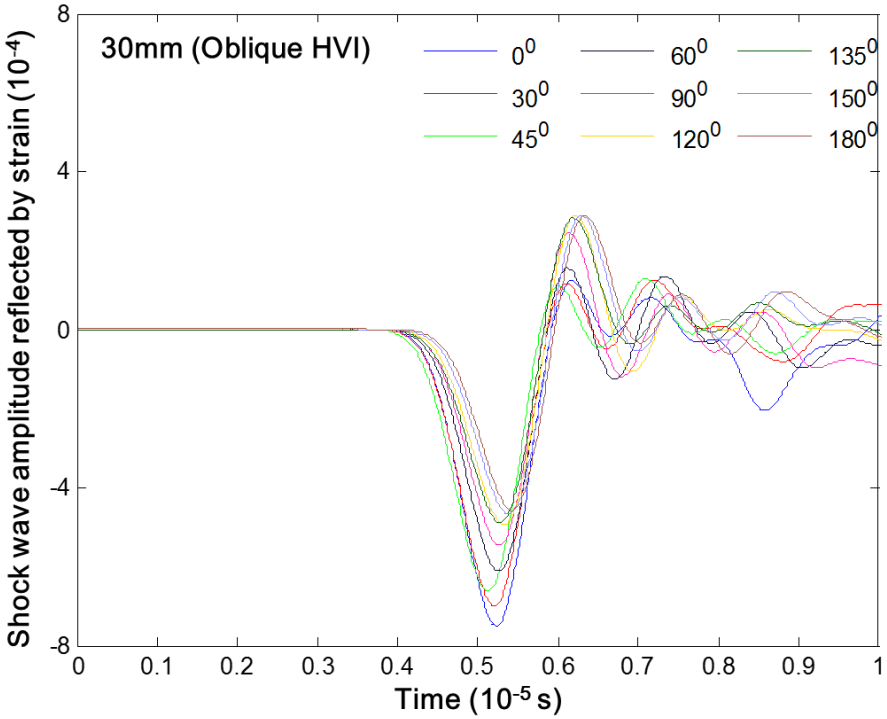

847

848 (b)

849 **Figure 10** In-plane strain in normal and oblique HVI acquired at gauge points with a wave
850 propagation distance of 30 mm from HVI spot at different wave propagation directions: (a) normal HVI
851 and (b) oblique HVI

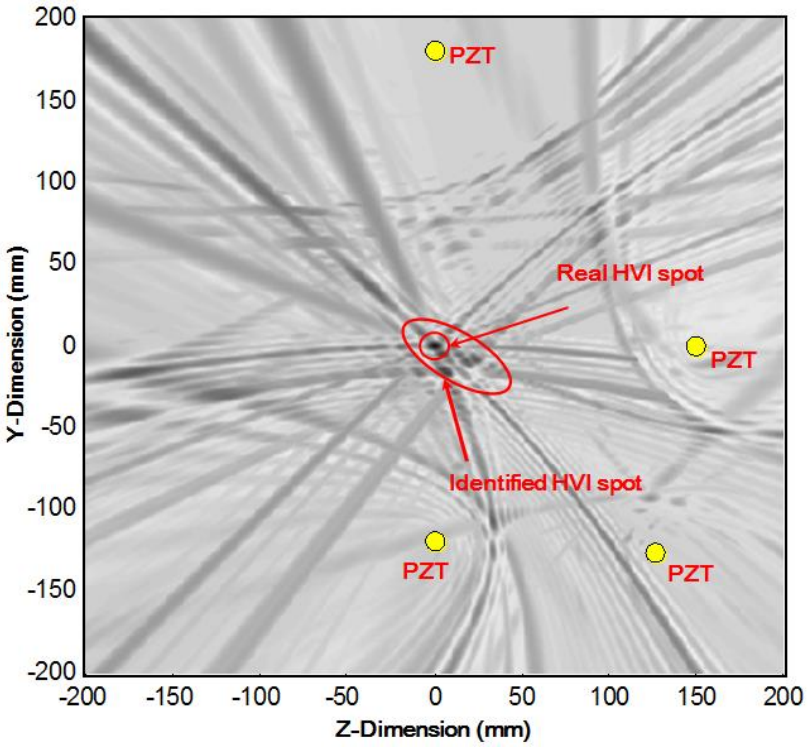

852

853 (a)

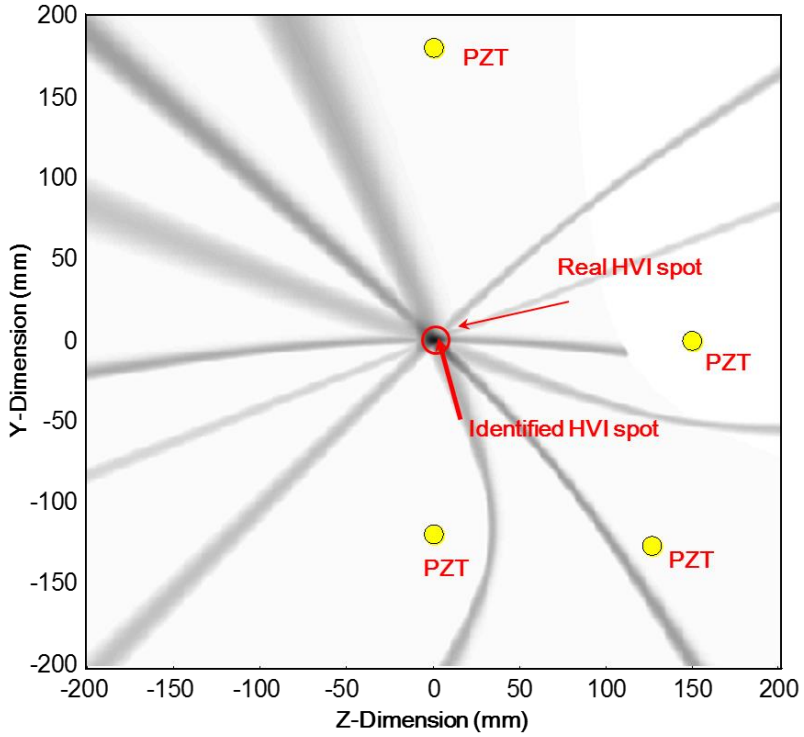

854

855 (b)

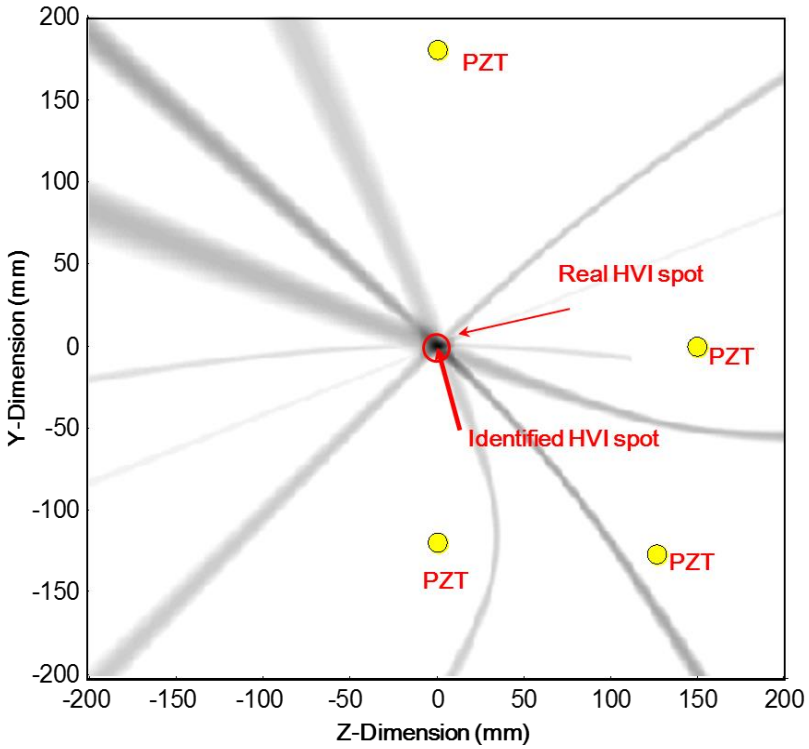

(c)

Figure 11 Ultimate resulting image with four sensors (a) in normal HVI without noise screening process (b) in normal HVI with noise screening process and (c) in oblique HVI with noise screening process